Analysis of the Contribution of Magnetic Moment Conservation to Ion Energy Transport in the GAMMA 10/PDX Divergent Field Region*)

Kosuke TAKANASHI, Satoshi TOGO, Naomichi EZUMI, Mafumi HIRATA, Tsukasa SUGIYAMA[1)], Naoki SHIGEMATSU, Takumi SETO, Takuma OKAMOTO, Satoshi TAKAHASHI, Kunpei NOJIRI[2)] and Mizuki SAKAMOTO

Plasma Research Center, University of Tsukuba, Tsukuba 305-8577, Japan
[1)]*Department of Fusion Science, The Graduate University for Advanced Studies, SOKENDAI, Toki 509-5292, Japan*
[2)]*National Institutes for Quantum Science and Technology, Naka 311-0193, Japan*

(Received 8 January 2023 / Accepted 26 June 2023)

We investigated the contribution of magnetic moment conservation to ion energy transport in the divergent magnetic field region, using the GAMMA 10/PDX end region to simulate scrape-off layer (SOL) plasmas in DEMO reactors. The averaged parallel energy increments ($\Delta E_{\parallel}$) were measured by performing energy analyses at two points: upstream and downstream of the GAMMA 10/PDX end region. A newly developed retarding field analyzer (RFA) was inserted upstream of the end region to perform energy analyses. Assuming that only effects of potential difference (ΔE_{ϕ}) and magnetic moment conservation ($\Delta E_{\langle\mu\rangle}$) affect $\Delta E_{\parallel}$, the contribution of magnetic moment conservation to ion energy transport was deduced. These results suggested that $\Delta E_{\langle\mu\rangle} < \Delta E_{\phi}$ irrespective of the difference in the diamagnetism at the central cell of GAMMA 10/PDX.

Keywords: energy transport, magnetic moment conservation, divergent magnetic field, SOL, retarding field analyzer

DOI: 10.1585/pfr.18.2402081

1. Introduction

Handling a large divertor heat load is a crucial issue in future fusion reactor DEMO. For example, more than 80% of the radiation fraction is thought required for JA DEMO, whereas approximately 50% is thought sufficient for ITER [1, 2]. Therefore, a deeper understanding and an accurate modeling of the transport processes of particles and energy are required.

Scrape-off layer (SOL) and divertor plasmas are mainly described using the Braginskii's plasma fluid model [3]. At the upstream of SOL plasmas in DEMO reactors, however, the collisionality is anticipated to not be sufficiently high for plasma fluid models to maintain their validity. As noted, in JA DEMO, the collisionality at the upstream of the SOL will be marginal and kinetic effects play an important role, particularly in ion energy transport [4]. This indicates that the diagnostics of kinetic information such as ion velocity distribution functions in SOL plasmas from experimental and theoretical perspectives will considerably improve of plasma fluid modeling.

Furthermore, in these low-to-marginal collisionality plasmas, ion temperature anisotropy is expected to be remarkable by kinetic particle-in-cell simulations [5]. In addition, SOL plasmas experience a finite inhomogeneity of magnetic field B during their parallel flows. The inhomogeneity of B in a tokamak SOL can be approximately estimated by $B_{\max}/B_{\min} \sim (R_0+a)/(R_0-a) = (1+\varepsilon)/(1-\varepsilon)$ by assuming that the magnetic field is dominated by toroidal field B_{t} and that B_{t} is inversely proportional to major radius coordinate R. Here, the maximum and minimum values of B are denoted by $B_{\max}$ and $B_{\min}$, respectively, and the inverse aspect ratio is defined by $\varepsilon \equiv a/R_0$ in terms of major radius R_0 and minor radius a of a tokamak. Even in the case of a normal aspect ratio tokamak $\varepsilon \sim 0.3$ such as JA DEMO, $B_{\max}/B_{\min}$ is estimated to be approximately 2. In this inhomogeneity of B with a remarkable ion temperature anisotropy, the mirror force term in the equation of the parallel ion flow, $(p_{\mathrm{i}\parallel} - p_{\mathrm{i}\perp})\nabla_{\parallel}B/B$, can be comparable with pressure gradient term $\nabla_{\parallel}p_{\mathrm{i}\parallel}$ [6]. The parallel and perpendicular ion pressures are denoted as $p_{\mathrm{i}\parallel}$ and $p_{\mathrm{i}\perp}$, respectively. However, in Braginskii's plasma fluid model, the ion temperature is described by an effective isotropic model, and the effects of the ion temperature anisotropy are addressed by an approximated model. Plasma fluid modeling with directly incorporating anisotropic ion pressures has demonstrated that the plasma profiles computed by it are qualitatively different from those computed by

author's e-mail: takanashi_kousuke@prc.tsukuba.ac.jp
*) This article is based on the presentation at the 31st International Toki Conference on Plasma and Fusion Research (ITC31).

the Braginskii model in low-collisionality plasmas [7, 8]. Therefore, the ion temperature anisotropy and accompanying mirror force, which originate from magnetic moment conservation, should be accurately considered in fluid descriptions for SOL plasmas in DEMO reactors.

The effects of magnetic moment conservation also play an important role in a future plasma thruster, VASIMR, because it utilizes the ion cyclotron range of frequency (ICRF) heating and a magnetic nozzle to convert its perpendicular ion energy into fast parallel ion flows [9]. In a linear experimental device, HITOP, with a magneto-plasma-dynamic arcjet, the heated perpendicular component of the ion energy is converted into a parallel component from measurements by two electrostatic energy analyzers (that is, Faraday cups) inserted upstream and downstream in the magnetic nozzle region [10]. In conditions such as tokamak SOL plasmas, where the electron temperature is comparable with the ion temperature, however, the parallel electric field also has a finite contribution to ion acceleration; thus, the contribution of the magnetic moment conservation must be distinguished from it.

We developed a retarding field analyzer (RFA) to investigate the contribution of magnetic moment conservation to ion energy transport in inhomogeneous magnetic field systems. In this study, we inserted it upstream, comparably strong magnetic field position (~ 1.2 T) within one of the end divergent field regions of a tandem mirror GAMMA 10/PDX [11–16]. In GAMMA 10/PDX, arrays of end-loss ion energy analyzers (ELIEAs) at both end plates have already been installed [11, 14, 15]. Therefore, a diagnostic condition similar to that described in Ref. [10] was reproduced, with an RFA at the upstream and an ELIEA at the downstream in the divergent magnetic field region. Because the plasmas in the end regions of GAMMA 10/PDX are almost collisionless and free from chemical reactions, they are considered useful when considering the effects of the divergent magnetic field on ion energy transport.

In this study, we deduced the contribution of the magnetic moment conservation to ion energy transport from parallel ion energy analyses using RFA and ELIEA. For a direct and correct evaluation, perpendicular ion energy analyses are essential; however, this remains as our future work. To actively alter the contribution of magnetic moment conservation to ion energy transport, we generated plasmas with different diamagnetism (DM) at the central cell (CC) by controlling the ICRF input power.

2. Experimental Device and Diagnostics

2.1 Development and installation of an RFA

Figure 1 (a) shows the newly developed RFA. The cylindrical chassis of the RFA has a diameter of 43 mm and a height of 44 mm. The diameter of the aperture is 6.5 mm. As shown in Fig. 1 (b), it consists of three grids

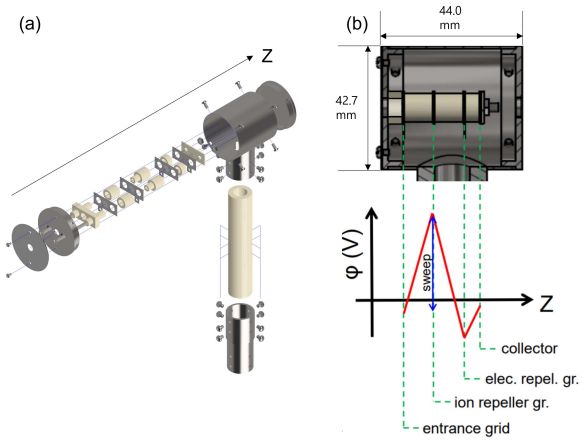

Fig. 1 (a) Schematics of the RFA, (b) side view of the RFA and applied voltages on the grids and collector plate.

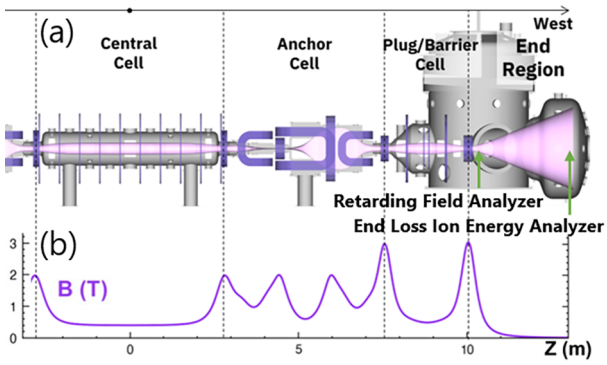

Fig. 2 (a) Schematic of the GAMMA 10/PDX tandem mirror western side with the positions of the RFA and the ELIEA indicated by arrows, and (b) magnetic field distribution of the GAMMA 10/PDX western side.

and a collector plate: a negatively biased (−200 V) entrance grid to repel electrons in the plasma, negative to positive biased (−150 to 550 V) ion repeller grid to discriminate the ion energy collected by the collector, negatively biased (−250 V) secondary electron repeller grid to return secondary electrons emitted from the collector, and negatively biased (−9 V) collector plate. The material and mesh size of the grids are Mo and 150 mesh/inch, respectively. Note that the plasma-facing plate and cover of the RFA are in floating potential, the absolute value of which is assumed to be one order of magnitude smaller than that of the entrance grid potential [15].

The voltage-current (VI) characteristics are obtained by sweeping the ion repeller voltage at 160 Hz.

Figure 2 shows a schematic of GAMMA 10/PDX and its magnetic field profile. Here, Z represents the coordinate along the magnetic axis. The RFA is inserted at $Z = 10.35$ m (on-axis $B \approx 1.2$ T), and the ELIEA is equipped on the end plate at $Z = 13.5$ m (on-axis $B \approx 0.0097$ T).

2.2 Experimental conditions

In the present experiments, plasmas with different DM

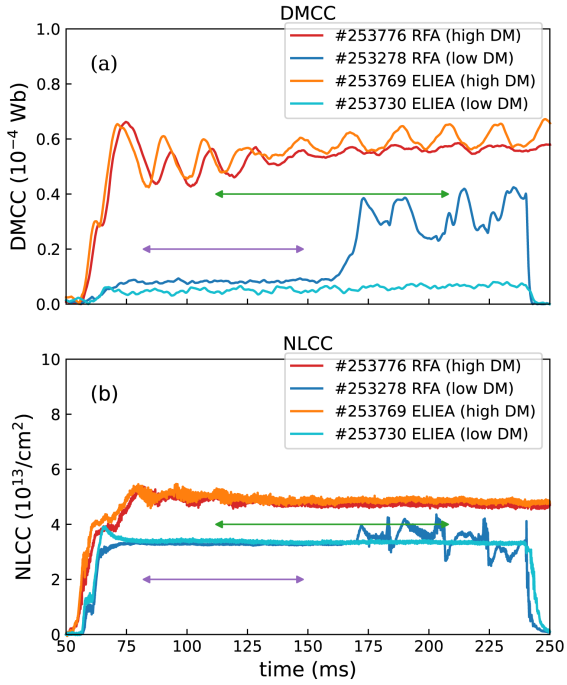

Fig. 3 (a) DMCC and (b) NLCC of the four analyzed discharges. Green and purple double-headed arrows indicate the time periods used for analyses in high and low DMCC cases, respectively.

are generated using the ICRF heating system, in a manner similar to that in Ref. [15]. Figure 3 shows the DM and line density in the CC, denoted as DMCC and NLCC, respectively, for the four plasma discharges analyzed in this study. Two of these (shot nos. 253769 and 253776) represent high DMCC ($\sim 0.5 \times 10^{-4}$ Wb) cases and the other two (shot nos. 253278 and 253730) represent low DMCC ($\sim 0.1 \times 10^{-4}$ Wb) cases. Note that the main contributor to the DMCC increase is the ion pressure increase, because the plasmas were heated only by the ICRF in the present study, although a finite electron drag exists. RFA and ELIEA measurements are not performed for a single plasma discharge because the upstream RFA may affect the downstream ELIEA measurements. However, Fig. 3 shows that the plasmas in the CC are maintained almost the same in each DMCC case. The RFA and ELIEA data are analyzed during discharge times of 110 - 210 ms for high DMCC cases and 80 - 150 ms for low DMCC cases, as indicated by the double-headed arrows in Fig. 3.

2.3 Analyses of the velocity distribution functions and fluid moment quantities

In both the RFA and ELIEA analyses, the VI characteristics during the rising-voltage phases within the analyzed time periods are averaged. The parallel-velocity distribution function, $f(v_\parallel)$, can be computed from the averaged VI characteristics using the following equation:

$$f(v_\parallel) = \mp \frac{m_\mathrm{i}}{e^2 S} \frac{\mathrm{d}I}{\mathrm{d}V}, \tag{1}$$

where $v_\parallel$ and m_i denote the parallel ion velocity and mass, respectively. The collector current and effective area are denoted by I and S. The sweeping voltage and elementary charge are denoted by V and e. Negative and positive signs correspond to the RFA and ELIEA, respectively.

To extract the fluid moment quantities from the averaged VI characteristics, we assume that $f(v_\parallel)$ can be approximated by double-shifted Maxwellians (sM) as follows:

$$f(v_\parallel) \approx f_1^{sM}(v_\parallel) + f_2^{sM}(v_\parallel), \tag{2}$$

$$f_{1(2)}^{sM}(v_\parallel) = n_{\mathrm{i}1(2)} \sqrt{\frac{m_\mathrm{i}}{2\pi T_{\mathrm{i}\parallel 1(2)}}} \exp\left(-\frac{m_\mathrm{i}(v_\parallel - u_{\parallel 1(2)})^2}{2T_{\mathrm{i}\parallel 1(2)}}\right). \tag{3}$$

Here, the subscripts 1 and 2 represent the components of $f(v_\parallel)$. The ion density, parallel ion flow, and parallel ion temperature are denoted by n_i, $u_\parallel$, and $T_{\mathrm{i}\parallel}$, respectively. In this study, ion heating is performed similarly to that described in Ref. [15], where two different ICRF antennas (RF1 and RF2) were used. RF2 resonates in the CC and RF1 resonates in the anchor cells. This generates double-component ion velocity distribution functions [14]. In addition, both the RFA and ELIEA observe end-loss ions that escape mirror confinement and have shifted velocity distributions. These are the physical backgrounds for the use of the double sM. Based on Eqs. (1) and (3), each component contributes to $I(V)$ as follows:

$$\begin{aligned} &I_{1(2)}^{RFA}(V) \\ &= \frac{1}{2} e S n_{\mathrm{i}1(2)} \sqrt{\frac{1}{\pi\beta_{1(2)}}} \left\{ \sqrt{\pi\beta_{1(2)}} u_{\parallel 1(2)} \right. \\ &\quad \cdot \left(1 + \mathrm{erf}\left(\sqrt{\beta_{1(2)}} \left(u_{\parallel 1(2)} - \sqrt{\frac{2eV}{m_\mathrm{i}}} \right) \right) \right) \\ &\quad \left. + \exp\left(-\beta_{1(2)} \left(u_{\parallel 1(2)} - \sqrt{\frac{2eV}{m_\mathrm{i}}} \right)^2 \right) \right\}, \end{aligned} \tag{4}$$

$$\begin{aligned} &I_{1(2)}^{ELIEA}(V) \\ &= \frac{1}{2} e S n_{\mathrm{i}1(2)} \sqrt{\frac{1}{\pi\beta_{1(2)}}} \left\{ \sqrt{\pi\beta_{1(2)}} u_{\parallel 1(2)} \right. \\ &\quad \cdot \left(\mathrm{erf}\left(\sqrt{\beta_{1(2)}} u_{\parallel 1(2)} \right) - \mathrm{erf}\left(\sqrt{\beta_{1(2)}} \left(u_{\parallel 1(2)} - \sqrt{\frac{2eV}{m_\mathrm{i}}} \right) \right) \right) \\ &\quad \left. - \exp\left(-\beta_{1(2)} \left(u_{\parallel 1(2)} - \sqrt{\frac{2eV}{m_\mathrm{i}}} \right)^2 \right) + \exp(-\beta_{1(2)} u_{\parallel 1(2)}^2) \right\}, \end{aligned} \tag{5}$$

where the error function is defined as $\mathrm{erf}(x) = (2/\sqrt{\pi}) \int_0^x \exp(-t^2)\mathrm{d}t$ and $\beta_{1(2)}$ is defined as $\beta_{1(2)} = m_\mathrm{i}/(2T_{\mathrm{i}\parallel 1(2)})$. The averaged VI characteristics measured by the RFA and ELIEA are then fitted using the following formulae:

$$I^{RFA}(V) = I_1^{RFA}(V) + I_2^{RFA}(V), \tag{6}$$

$$I^{ELIEA}(V) = I_1^{ELIEA}(V) + I_2^{ELIEA}(V). \tag{7}$$

Table 1 Six fitting parameters obtained as a result of the fittings of Eqs. (6) and (7) to the averaged VI characteristics.

shot no.	n_{i1} (10^{15} m^{-3})	$u_{\parallel 1}$ (10^5 m/s)	$T_{i\parallel 1}$ (eV)	n_{i2} (10^{15} m^{-3})	$u_{\parallel 2}$ (10^5 m/s)	$T_{i\parallel 2}$ (eV)
#253776 high DM (RFA)	1.2	0.99	23	1.1	1.8	70
#253769 high DM (ELIEA)	0.097	1.8	15	0.019	3.5	64
#253278 low DM (RFA)	1.8	1.1	28	1.1	1.0	94
#253730 low DM (ELIEA)	0.087	1.8	18	0.018	1.8	54

Table 2 Fluid moment quantities evaluated by the RFA and ELIEA. The asterisks indicate that n_i by the RFA is evaluated from Eq. (13).

shot no.	n_i (10^{15} m^{-3})	$u_\parallel$ (10^5 m/s)	$T_{i\parallel}$ (eV)
#253776 high DM (RFA)	22*	1.4	62
#253769 high DM (ELIEA)	0.12	2.1	61
#253278 low DM (RFA)	22*	1.0	53
#253730 low DM (ELIEA)	0.10	1.8	24

The effective values of n_i, $u_\parallel$, and $T_{i\parallel}$ are calculated as follows:

$$n_i = n_{i1} + n_{i2}, \tag{8}$$

$$u_\parallel = c_1 u_{\parallel 1} + c_2 u_{\parallel 2}, \tag{9}$$

$$T_{i\parallel} = 2E_\parallel - m_i u_\parallel^2, \tag{10}$$

$$E_\parallel = c_1 E_{\parallel 1} + c_2 E_{\parallel 2}, \tag{11}$$

$$E_{\parallel 1(2)} = \frac{1}{2} m_i u_{\parallel 1(2)}^2 + \frac{1}{2} T_{i\parallel 1(2)}, \tag{12}$$

where $c_{1(2)} = n_{i1(2)}/n_i$. The average parallel ion kinetic energy is denoted by $E_\parallel$. Because the exact evaluation of n_i by the RFA is difficult owing to the effects of the transmissivity of the grids, we replace n_i by the RFA with n_i^* by assuming particle continuity as follows:

$$\left(\frac{n_i^* u_\parallel}{B}\right)^{RFA} = \left(\frac{n_i u_\parallel}{B}\right)^{ELIEA}. \tag{13}$$

The SciPy.optimize.curve_fit function is used to fit Eqs. (6) and (7) for the VI characteristics. For the RFA analyses, owning to the non-negligible noise in the VI characteristics, the resulting fitting parameters have a finite dependency on the initial values. A sensitivity analysis of the initial values shows that a 10% variation in one of the initial values results in at most a 10% variation in the fitting parameters (as shown in Table 1). However, the variations in the effective quantities, as shown in Table 2, that are used to analyze the contribution of magnetic moment conservation, are maintained less than 5%. In addition, as demonstrated in Section 3, Eqs. (6) and (7) fit the VI characteristics well. Therefore, this initial value dependency does not affect the conclusions, either qualitatively or semi-quantitatively.

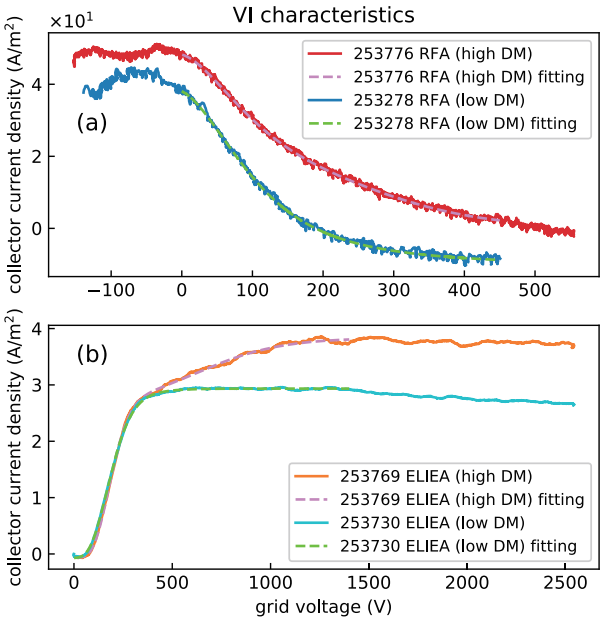

Fig. 4 Averaged VI characteristics measured by the (a) RFA and (b) ELIEA, and fitting curves (Eqs. (6) and (7)) to them.

3. Experimental Results

Figure 4 shows the averaged VI characteristics measured using the RFA and ELIEA. For the RFA results in the low DMCC case, $I < 0$ was observed. Notably, a finite number of electrons reached the collector plate overcoming the entrance retarding field (−200 V). Improving this aspect is one of our future studies, and we dealt with this negative current as an offset in this study. Equations (6) and (7) fitted well to the averaged VI characteristics, indicating that $f(v_\parallel)$ was well approximated by a double sM in the present study. The six fitting parameters used in Eqs. (4) and (5) are presented in Table 1.

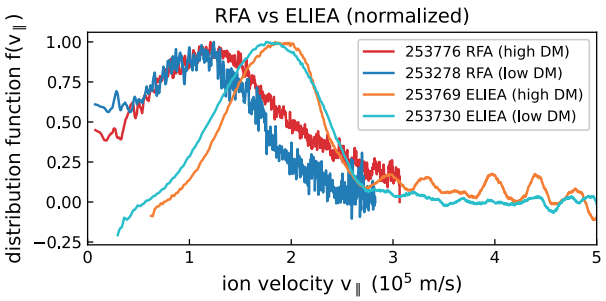

Fig. 5 Parallel ion velocity distribution function $f(v_\parallel)$ obtained from the RFA and ELIEA measurements.

Notably, in the high DMCC cases, the parallel ion flow of high-temperature component $u_{\parallel 2}$ became considerably faster than that of low-temperature component $u_{\parallel 1}$. Table 2 lists the fluid moment quantities evaluated using Eqs. (8) - (13). Note here that $T_{i\parallel}$ evaluated by the ELIEA in this study was one order lower than that in earlier studies [11, 14, 15] because $T_{i\parallel}$ evaluated in earlier studies by linear fittings to single-logarithm VI curves was not local $T_{i\parallel}$ but rather related to $T_{i\parallel}$ in the CC [17]. Notably, $T_{i\parallel}$ decreased from the RFA to the ELIEA positions. This is believed to be due to adiabatic expansion in the accelerating flow field. We also evaluated the increments in $E_\parallel$. In the high DMCC cases, $E_\parallel$ increased by 132 eV from the RFA to the ELIEA positions. In the low DMCC cases, $E_\parallel$ increased by 97 eV from the RFA to the ELIEA positions.

As shown in Table 2, the differences in the fluid moment quantities between the high and low DMCC cases were small, despite the remarkable difference in DMCC. This is visually demonstrated in Fig. 5 that shows $f(v_\parallel)$ evaluated from the RFA and ELIEA based on Eq. (1). This showed that $f(v_\parallel)$ for the low and high DMCC cases at each position almost overlapped. Therefore, the contribution of the parallel electric field almost masked that of the magnetic moment conservation in the end region of GAMMA 10/PDX in the present study.

Note here that Fig. 5 shows $f(v_\parallel)$ evaluated from the RFA having finite values in the slow range ($v_\parallel < 0.5 \times 10^5$ m/s). We believe that these slow-velocity ions would not exist in the end-loss ions when the RFA is not inserted, but might be produced from recycling neutrals on the plasma-facing plate of the RFA. Specifying the origin of these slow-velocity ions is also an issue for future research.

4. Discussion

We assumed here that the increment in $E_\parallel$ ($\Delta E_\parallel$) was caused only by the effects of the parallel electric field (ΔE_ϕ) and magnetic moment conservation ($\Delta E_{\langle\mu\rangle}$), that is, $\Delta E_\parallel = \Delta E_\phi + \Delta E_{\langle\mu\rangle}$. As mentioned in Section 1, perpendicular ion energy analyses are essential to evaluate $\Delta E_{\langle\mu\rangle}$ but they remain as our future works. To evaluate ΔE_ϕ, we assumed that the profile of the electrostatic potential, ϕ,

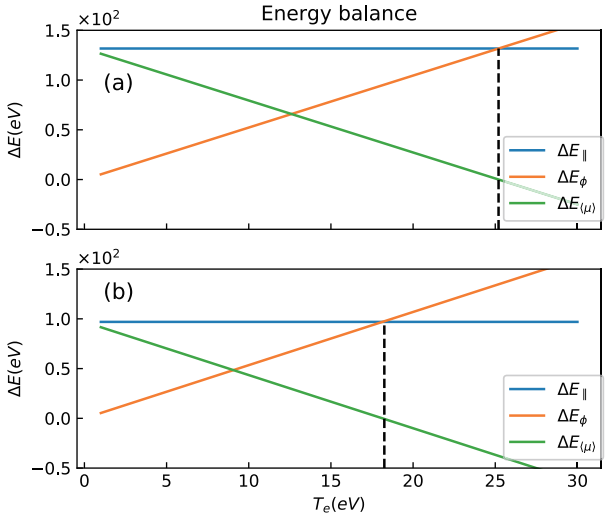

Fig. 6 Contributions of parallel electric field ΔE_ϕ and magnetic moment conservation $\Delta E_{\langle\mu\rangle}$ in the increments of average parallel ion kinetic energy $\Delta E_\parallel$ for the (a) high and (b) low DMCC cases. The vertical broken lines indicate the maximum possible T_e in the present discussion.

obeys the Boltzmann relationship as follows:

$$\Delta\phi = \frac{T_e}{e} \ln\left(\frac{n_i^*}{n_i^{ELIEA}}\right). \quad (14)$$

Here, electron temperature T_e was assumed to be isothermal. T_e was not measured during the plasma discharges studied in this research; therefore, we assumed it to be a variable in this discussion.

Figure 6 shows the balance between ΔE_ϕ and $\Delta E_{\langle\mu\rangle}$ for the high and low DMCC cases as functions of T_e. Based on the assumptions in this discussion, T_e could not exceed $\sim$ 25 eV and $\sim$ 18 eV in the high and low DMCC cases (indicated in Fig. 6 by the vertical broken lines), respectively. Langmuir probe measurements of T_e performed in the end region in earlier studies [15,16] indicated that T_e = 20 - 30 eV for DMCC = 0.1 - 0.5 $\times 10^{-4}$ Wb and had slight parallel gradients. Therefore, T_e lay in a side where ΔE_ϕ was larger than $\Delta E_{\langle\mu\rangle}$ in both cases. This supported the fact, as specified in Section 3, that the difference in DMCC did not cause large differences in the fluid moment quantities in the end region. This also indicated that the potential difference in the end region was on the order of 100 V. This qualitatively agreed with a recent numerical simulation result based on a plasma fluid model incorporating anisotropic ion pressures [18].

5. Summary

Parallel ion energy analyses were performed using the RFA and ELIEA in the end regions of GAMMA 10/PDX. The contribution of magnetic moment conservation to ion energy transport was deduced by assuming that only the potential difference and magnetic moment conservation affected the parallel energy increment. These results sug-

gested that the effect of magnetic moment conservation on energy transport was not as large as the effect of the potential difference; this supports the fact that no significant differences exist in the fluid moment quantities, irrespective of the difference in DMCC. For a more accurate evaluation of the contribution of the magnetic moment conservation to ion energy transport, we plan to perform perpendicular ion energy analyses. Electron temperature measurements are necessary to determine the contribution of the parallel electric field. We also plan to improve the accuracy of the RFA measurement by addressing the negative current observed in the low DMCC case and evaluating the effective transmittivity of the grids.

Acknowledgements

The authors are grateful to Prof. U. Czarnetzki and Dr. T.V. Tsankov of Ruhr Universität Bochum, and Prof. T. Takizuka of Osaka University for productive discussions. This study was partly supported by the bidirectional collaborative research program of the National Institute for Fusion Science, Japan (NIFS20KUGM148 and NIFS21KUGM164). We would like to thank Editage (www.editage.jp) for English language editing.

[1] N. Asakura *et al.*, Nucl. Fusion **57**, 126050 (2017).
[2] N. Asakura *et al.*, Nucl. Mater. Energy **26**, 100864 (2021).
[3] S.I. Braginskii, *Reviews of Plasma Physics*, vol.**1** (Consultants Bureau, New York, 1965) p.205.
[4] Y. Homma, Plasma Phys. Control. Fusion **64**, 045020 (2022).
[5] A. Froese *et al.*, Plasma Fusion Res. **5**, 026 (2010).
[6] W. Fundamenski, Plasma Phys. Control. Fusion **47**, R163 (2005).
[7] S. Togo *et al.*, Plasma Fusion Res. **13**, 3403022 (2018).
[8] S. Togo *et al.*, Plasma Fusion Res. **18**, 1203005 (2023).
[9] F.R. Chang-Dıaz, Thin Solid Films **506-507**, 449 (2006).
[10] M. Inutake *et al.*, Plasma Phys. Control. Fusion **49**, A121 (2007).
[11] Y. Nakashima *et al.*, Nucl. Fusion **57**, 116033 (2017).
[12] M. Sakamoto *et al.*, Nucl. Mater. Energy **12**, 1004 (2017).
[13] N. Ezumi *et al.*, Nucl. Fusion **59**, 066030 (2019).
[14] K. Ichimura *et al.*, Plasma Fusion Res. **7**, 2405147 (2012).
[15] K. Nojiri *et al.*, Plasma Fusion Res. **14**, 2401086 (2019).
[16] Y. Kinoshita *et al.*, Plasma Fusion Res. **14**, 2402063 (2019).
[17] J.H. Foote and G.D. Porter, Plasma Phys. Control. Fusion **31**, 255 (1989).
[18] S. Togo *et al.*, J. Adv. Simulat. Sci. Eng. **9**, 185 (2022).